

Numerical analysis of the influence of magnetic field waveforms on the performance of active magnetic regenerators

Fábio P. Fortkamp · Gusttav B. Lang · Jaime A.

Lozano · Jader R. Barbosa Jr.

Abstract Magnetic cooling is an alternative to vapor compression with no use of hazardous gases. The refrigerant is a solid material which reacts to oscillations in magnetic field with changes in temperature. In active magnetic regenerators, this magnetocaloric material and its effect are coupled with an oscillating fluid flow to yield a thermodynamic cooling cycle between cold and hot source temperatures. The literature is abundant with studies on the influence of the fluid flow waveform on magnetic refrigeration devices, but the influence of the magnetic field waveform is less investigated. In this work, we simulate a previously developed active magnetic regenerator numerical model with different mathematically-defined waveforms, and determine which operating parameters yield the highest values for cooling capacity and coefficient of performance. Results show that the highest performance levels are achieved when the magnetic field is kept constant for the same duration of the fluid flow

Fábio P. Fortkamp

E-mail: fabio@polo.ufsc.br

Gusttav B. Lang · Jaime A. Lozano · Jader R. Barbosa Jr.

POLO — Research Laboratories for Emerging Technologies in Cooling and Thermophysics, Department of Mechanical Engineering, Federal University of Santa Catarina, Florianópolis, SC, 88040-900, Brazil

through the magnetized material, and that the transition times between high and low levels of the magnetic field should be as fast as possible.

Keywords magnetic refrigeration · active magnetic regenerator · numerical modeling · magnetocaloric effect

List of symbols

Variables

A_{sf}	contact surface area between solid and fluid phases in the regenerator [m^2]
A_t	amplitude of the pressure gradient waveform in the fluid momentum equation [m/s]
c	specific heat [$J/(kg K)$]
c_E	Ergun constant of the porous medium
COP	coefficient of performance
D_{ld}	dispersion term in the AMR model [m/s^2]
f	cycle frequency [Hz]
F_M	magnetization fraction
$g(t)$	dimensional waveform of the pressure gradient term in the fluid momentum equation
\hbar	heat transfer coefficient [$W/(m^2 K)$]
K	permeability of the porous medium [m]
k^{eff}	effective thermal conductivity [$W/(m K)$]
\dot{m}_f	mass flow rate [kg/s]
M	magnetization field [A/m]
m	mass [kg]
N_D	demagnetization tensor

N_r	number of regenerators
N_v	number of valves
ΔP	pressure drop across one region [Pa]
P	pressure [Pa]
\dot{q}_{csg}	volumetric casing losses in the AMR model [W/m ³]
T	temperature [K]
t	time [s]
V	velocity [m/s]
$\dot{W}_{\text{relay},n}$	nominal power consumption of one relay [W]
\dot{W}_{valve}	valve power [W]
$\dot{W}_{\text{valve},n}$	nominal power consumption of one valve [W]
\dot{W}_{mag}	magnetic power [W]
\dot{W}_{pump}	pumping power [W]
z	axial coordinate [m]
θ_R	ramp rate in the magnetic ramp profile
τ_M	magnetization period in the magnetic ramp profile [s]
τ_R	ramp period in the magnetic ramp profile [s]

Greek symbols

β	surface area density [m/m ³]
ε	porosity
Φ	utilization factor
Φ	utilization
ρ	density [kg/m ³]
ΔT_{ad}	adiabatic temperature variation [K]
τ	time period [s]

τ_B	blow duration [s]
μ	dynamic viscosity [Pa s]

Subscripts and Superscripts

air	air layer between magnets and regenerators
csg	regenerator casing
csg	regenerator casing
f	fluid phase
s	solid phase
sf	relative to the heat transfer between solid and fluid phases in the regenerator

Abbreviations

C	cold source
CC	cold cycle
CE	cold end
H	hot source
HB	hot blow
HC	hot cycle
IT	instantaneous magnetic profile
AMR	Active Magnetic Regenerator
MCE	Magnetocaloric Effect
MCM	Magnetocaloric Material
MR	Magnetic (or Magnetocaloric) Refrigeration
RC	rectified cosine magnetic profile
RM	rectified cosine magnetic profile

1 Introduction

Mechanical vapor compression has been the dominant cooling technology for the past century [1] but, despite its dominance, it still faces an increasing number of challenges related to its environmental footprint. In particular, the phase-out of refrigerants with ozone depleting and global warming potentials has introduced the use of flammable substances, with their own set of risks for consumer applications [2] and technological challenges [3].

Magnetic refrigeration (MR) is an advanced cooling technology with no use of hazardous gases, where a *magnetocaloric material* (MCM) is subjected to a cyclical change of the applied magnetic field, and its temperature changes as a result of the *magnetocaloric effect* (MCE). The magnitude of the MCE depends on material parameters, magnetic field variation and temperature, and is maximal at the Curie temperature of the material. For a thorough introduction to the magnetocaloric effect and magnetocaloric materials, the reader is referred to [4].

For operating conditions typical of a low-temperature span magnetic refrigerator, the MCE is typically on the order of 2-5 K. To amplify this temperature change, heat regeneration is usually employed [5]. Active magnetic regenerators (AMR) are thermal devices where the magnetocaloric material constitutes a solid matrix through which flows an aqueous heat transfer fluid, and which is cyclically magnetized and demagnetized to activate the magnetocaloric effect. Such a regenerator is essentially a cascade of infinitesimal “layers” of MCM that are activated simultaneously to build up a temperature profile along its length. These layers can be made of the same material, yielding an homogeneous regenerator; however, given the dependence of the MCE with temperature, it is an interesting strategy to build *multilayer* regenerators, where each layer is composed of a different material that will work around its own Curie temperature, maximizing the magnetocaloric effect of each portion.

Magnetic refrigerators can operate according to different thermodynamic cycles, but the stages are roughly as follows. The magnetic circuit magnetizes the MCM, increasing its temperature due to the MCE. During the so-called *cold blow*, cold fluid from the cold source flows through the warm bed and absorbs its energy, releasing it to the external heat exchanger. On the return of the fluid, the solid is demagnetized and cooled down, and in the *hot blow* the fluid releases energy to the bed, decreasing its temperature so it can absorb the thermal load at the cold source. The cycle then repeats; different cycles can be configured by different durations and synchronization steps between these two *characteristic waveforms*:

1. The *magnetic profile*, which describes the oscillating magnetic field over one regenerator;
2. The *fluid flow profile*, which describes the time-variation of flow rate through one bed.

Fluid flow profiles are more easily investigated with experimental methods, since they can be altered with modifications in the fluid flow system. In particular, the *duration* of blows have been extensively investigated [6,7,8], and the literature shows that the cooling capacity of magnetic refrigerators can be increased by focusing fluid flows during periods where the magnetic field is at its extrema values.

In this work, we focus on magnetic profiles, which are less studied in the literature. These waveforms are usually investigated in terms of their synchronization with the fluid flow profile [9,10]. This paper uses the AMR model developed by [11], and the same authors had studied magnetic profiles waveforms in an earlier work [12]. However, their amplitudes was not varied, nor were they investigated with different geometries.

The present work combines the gaps from the above cited papers in investigating the performance of a magnetic refrigerator under different magnetic profile waveforms. These waveforms are mathematically modeled, and the cooling capacity and coefficient of per-

formance are calculated based on the profiles parameters, while also investigated how the AMR geometry affect the performance in combinations with the magnetic profile. The fluid flow profile is assumed fixed in shape, although its parameters are also varied. To emulate constraints on an operating point of actual magnetic refrigeration devices, the temperature span is set fixed, and hence few comments are made on second-law efficiency.

2 Materials and methods

As previously explained, we perform numerical simulations of a previously developed AMR model, varying the profile-specific and geometric parameters. We also couple a model for calculating the power consumption of a proposed fluid management system, a topic understudied in the literature. The output of this integrated model are cooling capacity, power contributions and the coefficient of performance (COP).

2.1 AMR model

2.1.1 Governing equations

Simulations were performed using a one-dimensional AMR mathematical model, implemented using the Finite Volumes Method [11]. Here we will show a summarized version focusing on the governing equations. This model solves momentum and energy balance equations for the solid and fluid phases, represented by indices ‘s’ and ‘f’, respectively. The model geometry is depicted in Figure 1, and assumes regenerators composed of monodisperse packed spheres with porosity ϵ .

The momentum equation for the fluid domain is:

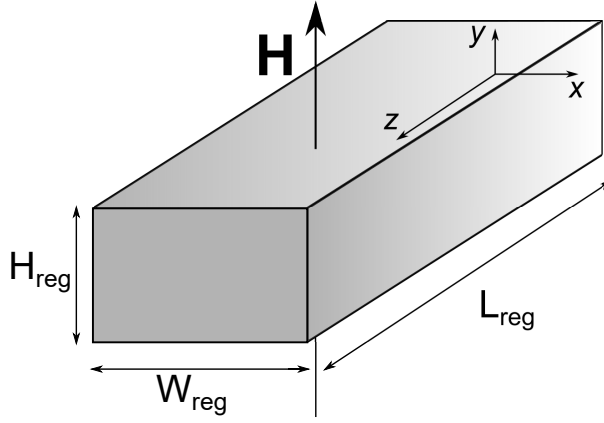


Fig. 1: AMR model geometry

$$\frac{\rho_f}{\varepsilon} \frac{\partial V_z}{\partial t} = -\frac{\partial P}{\partial z} - \frac{\mu_f}{K} V_z - \frac{c_E \rho_f}{K^{1/2}} |V_z| V_z \quad (1)$$

and is solved for the time-dependent uniform fluid velocity V_z through the bed.

The energy equation for the fluid phase can be written as:

$$\begin{aligned} \rho_f c_{p,f} \left(\varepsilon \frac{\partial T_f}{\partial t} + V_z \frac{\partial T_f}{\partial z} \right) = & -\dot{h}_{sf} \beta (T_f - T_s) \\ & + \left| V_z \frac{\partial P}{\partial z} \right|_f \\ & + \varepsilon \left(k_f^{\text{eff}} + \rho_f c_{p,f} D_{ld} \right) \frac{\partial^2 T_f}{\partial z^2} \\ & + \dot{q}_{csg} \end{aligned} \quad (2)$$

while the energy equation for the solid phase is written as:

$$\rho_s c_s (1 - \varepsilon) \frac{\partial T_s}{\partial t} = \dot{h}_{sf} \beta (T_f - T_s) + (1 - \varepsilon) k_s^{\text{eff}} \frac{\partial^2 T_s}{\partial z^2} \quad (3)$$

Initial and boundary conditions, solution methods, convergence analyses, and closure relations for the porous media terms are described in [11]. This AMR model solves the above

equations for one regenerator operating between given sources temperatures (assuming ideal heat exchangers in contact with the thermal reservoirs), during one full cycle (hot and cold blows and magnetization and demagnetization periods), given specified operating conditions (to be discussed later).

The casing heat transfer term \dot{q}_{csg} in Equation 2 is calculated solving the heat conduction in the regenerators casing [11], and can be neglected to simplify some analyses. More details are provided in section 3.

2.1.2 How the fluid flow profile is used

The pressure gradient in Equation 1 is modeled as:

$$-\frac{\partial P}{\partial z} = \rho_f A_t g(t) \quad (4)$$

where $g(t)$ is a dimensionless function that expresses the mathematical waveform of the pressure gradient, and A_t is its amplitude, adjusted in a convergence loop; the mass flow rate calculated from the Darcy velocity from Equation 1 is compared with the input value of mass flow rate until these values converge. The waveform $g(t)$ represents the fluid flow profile used.

The canonical fluid flow profile considered in this work is the square wave or *instantaneous profile*, because of the instantaneous change in flow rate, as shown in Figure 2.

The instantaneous mass flow rate, $\dot{m}_f(t)$, is defined over a cycle with a period τ , and represents the fluid flow through a given regenerator bed. The so-called *hot cycle*, during which the MCM is magnetized, occupies the time interval $0 \leq t < \tau/2$, while the *cold cycle* lies between $\tau/2 \leq t \leq \tau$. The flow profile oscillates between two plateaus of equal magnitude $\dot{m}_{f,\text{max}}$ and opposite directions, which are centered in each half-cycle. During the hot cycle,

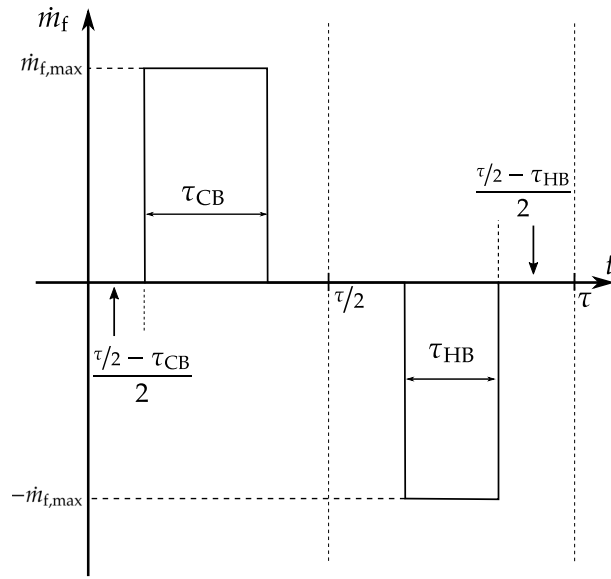


Fig. 2: Instantaneous fluid flow profile

the cold blow period is τ_{CB} , and during the cold cycle the hot blow period is τ_{HB} . If the flow is balanced, then $\tau_{CB} = \tau_{HB}$.

During each half cycle, there are periods without fluid flow, defined as:

$$\tau_{0,HC} = \frac{\tau/2 - \tau_{CB}}{2} \quad (5)$$

$$\tau_{0,CC} = \frac{\tau/2 - \tau_{HB}}{2} \quad (6)$$

where HC and CC stand for hot cycle and cold cycle, respectively.

The profile can be mathematically defined as:

$$\dot{m}_f(t) = \begin{cases} 0, & 0 \leq t < \tau_{0,HC} \\ \dot{m}_{f,max}, & \tau_{0,HC} \leq t \leq \tau/2 - \tau_{0,HC} \\ 0, & \tau/2 - \tau_{0,HC} < t < \tau/2 + \tau_{0,CC} \\ -\dot{m}_{f,max}, & \tau/2 + \tau_{0,CC} \leq t \leq \tau - \tau_{0,CC} \\ 0, & \tau - \tau_{0,CC} < t < \tau \end{cases} \quad (7)$$

When the blows have different time durations, the AMR cycle is considered unbalanced, and this is known to have a negative effect on performance [13, 7]. In this work, the blows are always balanced, hence the blow fraction, the ratio of blow durations to cycle period [7], can be evaluated as:

$$F_B = \frac{2\tau_B}{\tau} \quad (8)$$

where τ_B is the duration of one blow.

2.1.3 How the magnetic profile is used

The magnetic profile is modeled by a waveform of magnetic field strength $H(t)$ applied perpendicular to the regenerators, as shown in Figure 1. The magnetic field is assumed uniform throughout the beds. The applied field is corrected from demagnetization effects to yield the effective field inside the regenerators:

$$H^{eff} = H - N_D M \quad (9)$$

where M is the magnetization field of the material, and N_D is a demagnetization factor.

The magnetocaloric effect is implemented in the so-called discrete approach [14]; every time the magnetic field changes, based on the input magnetic profile, the solid temperature is calculated according to:

$$T_s(t + \Delta t) = T_s(t) + \Delta T_{\text{ad}} \left(T_s(t), H^{\text{eff}}(t), H^{\text{eff}}(t + \Delta t) \right) \quad (10)$$

where the adiabatic temperature variation ΔT_{ad} , a standard measure of the MCE, is calculated from tabulated experimental data for magnetocaloric materials as function of temperature and effective field. [11].

The magnetic profiles considered in this work are presented in terms of the flux density $B = \mu_0 H$, where μ_0 is the permeability of free space; the magnetic field H is used in the evaluation of the magnetocaloric effect (cf. Sec. 2.1.3).

The instantaneous profile (represented by the subscript “IT”) and the rectified cosine profile (represented by “RC”) are defined solely in terms of the extreme values B_{min} and B_{max} , and are shown in Figure 3.

$$B_{\text{IT}}(t) = \begin{cases} B_{\text{max}}, & 0 \leq t < \tau/2 \\ B_{\text{min}}, & \tau/2 \leq t < \tau \end{cases} \quad (11)$$

$$B_{\text{RC}}(t) = B_{\text{min}} + (B_{\text{max}} - B_{\text{min}}) \left| \cos \left(\frac{\pi}{\tau} \left(t - \frac{\tau}{4} \right) \right) \right| \quad (12)$$

A suitable approximation of the instantaneous profile is the *magnetic ramp profile*, shown in Figure 4, with finite transition times between the levels of constant magnetization. The magnetic profile oscillates between a low value B_{min} and a high value B_{max} , and remains at each plateau for a period of τ_{M} . The plateaus are balanced and centered at each half-cycle.

The *ramp period* τ_{R} is defined as:

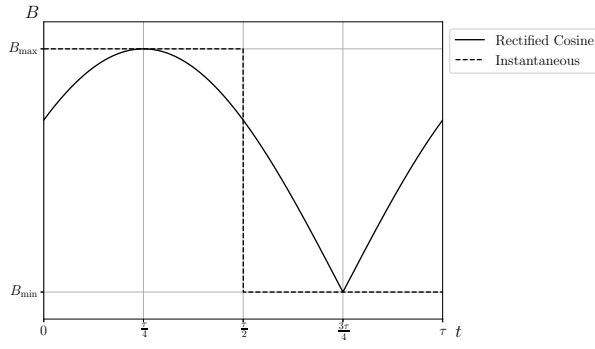


Fig. 3: Instantaneous ("IT") and rectified cosine ("RC") magnetic profiles

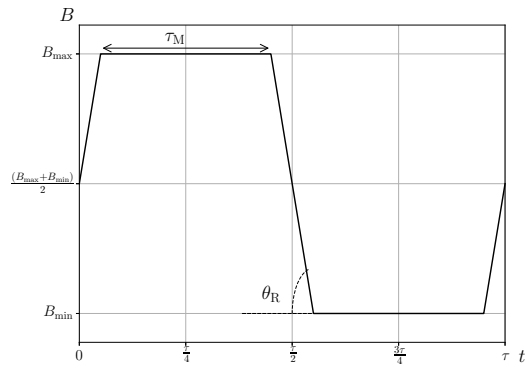


Fig. 4: Magnetic ramp profile

$$\tau_R = \frac{1}{4}(\tau - 2\tau_M) \quad (13)$$

such that there are four ramp periods in one full cycle. The ramp rate, θ_R , is:

$$\tan \theta_R = \frac{(B_{\max} - B_{\min})}{2\tau_R} \quad (14)$$

The magnetization fraction, F_M , is the fraction of the cycle during which the magnetocaloric material is subjected to a constant magnetic field:

$$F_M = \frac{2\tau_M}{\tau} \quad (15)$$

The ramp profile (“RM”) can be mathematically defined as:

$$B_{RM}(t) = \begin{cases} (B_{\max} + B_{\min})/2 + t \tan \theta_R, & 0 \leq t < \tau_R \\ B_{\max}, & \tau_R \leq t < \tau/2 - \tau_R \\ B_{\max} - (t - (\tau/2 - \tau_R)) \tan \theta_R, & \tau/2 - \tau_R \leq t < \tau/2 + \tau_R \\ B_{\min}, & \tau/2 + \tau_R \leq t < \tau - \tau_R \\ B_{\min} + (t - (\tau - \tau_R)) \tan \theta_R, & \tau - \tau_R \leq t \leq \tau \end{cases} \quad (16)$$

Additionally, the average values of the magnetic field during each half-AMR cycle are considered for comparison between profiles. The average magnetic profile during the hot cycle ($0 \leq t < \tau/2$) is denoted \bar{B}_{high} and the average during the cold cycle ($\tau/2 \leq t < \tau$) is denoted \bar{B}_{low} . For the instantaneous waveform, these average values are identical to the extrema values.

2.1.4 Evaluation of solid and fluid properties

The fluid properties are considered constant in the momentum equation to decouple the solution procedures to determine the velocity and temperature fields. The properties are computed at the average temperature between the hot and cold sources temperatures, and are evaluated from interpolated tables exported from the EES software [15]. In all simulations shown in this work, the heat transfer fluid is a mixture of water/ethylene-glycol with concentration 80/20 % vol. For the energy equations, the fluid properties are also calculated from tabulated data, but the temperature dependence is considered.

In this work, both single- and multilayer regenerators are considered. Single-layer regenerators are composed of gadolinium, a benchmark material with a Curie temperature of 290 K. For simplicity, the solid density is assumed constant at $\rho_s = 7900 \text{ kg/m}^3$ and the solid thermal conductivity is set to $k_s = 10.5 \text{ W/(mK)}$. The specific heat capacity of Gd is calculated as a function of temperature and magnetic field based on experimental data, using a bi-linear interpolation scheme; more details on the experimental dataset are available in [11].

For the multilayer simulations, alloys of gadolinium and yttrium are used in the form $\text{Gd}_{1-x}\text{Y}_x$, where x is the yttrium fraction. This fraction decreases the Curie temperature of the alloy relative to that of pure gadolinium. Due to the lack of experimental data on the magnetocaloric properties of $\text{Gd}_{1-x}\text{Y}_x$ alloys at the time this analysis was made, a simpler approach was used in which the properties of alloys with a low yttrium fraction are identical to those of pure gadolinium, except for the Curie temperature (which is shifted to lower values).

2.1.5 Performance metrics

The AMR model considers only one bed and assumes N_r identical beds experience the same cycle, multiplying the performance metrics below by this factor.

The cooling capacity is calculated as [11]:

$$\dot{Q}_C = N_r \frac{1}{\tau} \int_{\tau_{\text{HB}}} \dot{m}_f(t) c_{p,f} (T_C - T_{f,\text{CE}}) dt \quad (17)$$

The magnetic power to operate the AMR cycle is modeled as the ideal Carnot power, ignoring most thermal irreversibilities:

$$\dot{W}_{\text{mag}} = \dot{Q}_C \frac{T_H - T_C}{T_C} \quad (18)$$

while the fluid friction irreversibility is accounted for in the calculation of the pumping power:

$$\dot{W}_{\text{pump}} = N_r \frac{1}{\tau} \int_0^\tau \frac{\dot{m}_f}{\rho_f} \Delta P dt \quad (19)$$

where ΔP is the total pressure drop through the regenerator.

2.2 Hydraulic system and fluid flow profile model

The hydraulic system to modulate this fluid flow through different regenerators at different time instants is composed of a pump and a set of electronic valves which can be precisely controlled to yield the desired blow durations. The electrical power consumed by the valve array is computed separately from other work contributions. An application of electronic valves in AMR devices has been presented by [16].

Due to evolving developments in our group, two types of valves are considered, as will be elaborated in section 3.

The first approach, called *Type B valves*, uses the model of [17], assuming that the individual consumption of each valve is independent of frequency and blow fraction. The valve power \dot{W}_{valve} can be computed as:

$$\dot{W}_{\text{valve}} = N_v F_B \left(\dot{W}_{\text{valve},n} + \frac{1}{2} \dot{W}_{\text{relay},n} \right) \quad (20)$$

where N_v is the number of valves, $\dot{W}_{\text{valve},n}$ is the measured average nominal power for one normally-closed electronic valve and $\dot{W}_{\text{relay},n}$ is the nominal power for one controlling relay. The factor $1/2$ is due to two valves being controlled by one relay.

In the second approach, *Type A* valves are used, with lower nominal power but that depends on frequency and blow fraction. For these valves, the valve power was experimentally correlated as:

$$\dot{W}_{\text{valve}} [\text{W}] = N_v (0.927f [\text{Hz}] + 1.023F_B + 0.226f [\text{Hz}]F_B - 0.037) \quad (21)$$

Equation (21) was correlated for blow fractions of 50 and 100 % and for frequencies in the range of 0.2–1.6 Hz, with an uncertainty on the order of 0.4 W for a single valve. The use of different valve types will be discussed among the presented results.

Independent of the valve type used, it is also assumed that this valve system can produce the fluid flow profile shown in Figure 2, where the displaced fluid mass during one blow in one regenerator bed is $\dot{m}_{f,\text{max}}F_B\tau/2$.

The *utilization factor* can then be calculated as:

$$\Phi = \frac{\dot{m}_{f,\text{max}}F_Bc_s}{2fm_sc_s} \quad (22)$$

For an even number of poles in the magnetic circuit, it may be advantageous to employ an odd number of regenerator beds to break the symmetry between the magnetic circuit and the beds, thus avoiding positions of equilibrium between magnetic forces which result in torque oscillations [18]. Additionally, in general, two valves per regenerator may be necessary (one at each end), to independently control the hot and cold blows for each bed and correct flow imbalance; thus, in all results in this work, the number of valves is calculated as:

$$N_v = 2N_r \quad (23)$$

2.3 Calculation of the coefficient of performance

The coefficient of performance takes the cooling capacity as the main output parameter from the AMR model, in addition to all previously cited power contributions:

$$\text{COP} = \frac{\dot{Q}_c}{\dot{W}_{\text{pump}} + \dot{W}_{\text{mag}} + \dot{W}_{\text{valve}}} \quad (24)$$

3 Results and Discussions

The analysis of magnetic profiles was performed in two different stages in the research of our group, as discussed below.

3.1 Comparison of instantaneous and rectified cosine profiles using a simplified model

In the first stage, the instantaneous and rectified cosine profiles are compared in the AMR model, considering monolayer regenerators without casing losses, and using Type B valves. The parameters used in all simulations are presented in Table 1.

When comparing the performances resulting from the application of the different magnetic profiles, the average magnetic field during the hot cycle will be considered the same; this implies a higher peak for the rectified cosine. For the cold cycle, two comparison methods are considered, as shown in Figure 5:

1. The minimum values for both profiles is the same;
2. The average value for both profiles during the cold cycle is the same.

For reference, in all simulations, the minimum value for the rectified cosine was fixed at $B_{\text{min,RC}} = 0.1 \text{ T}$. In the first comparison, the minimum value for the instantaneous waveform was kept at the same level ($B_{\text{min,IT}} = B_{\text{min,RC}}$); hence, the average low value for the RC

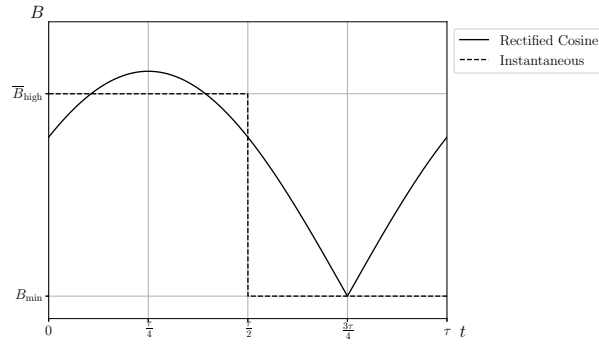
Table 1: AMR parameters kept fixed in the simulations with different magnetic profiles

Parameter	Value
D_p	0.5 mm
H_r	20 mm
W_r	25 mm
L_r	100 mm
N_r	11
N_v	22
T_H	298 K
T_C	278 K
\dot{W}_{NV}	4 W
\dot{W}_R	0.36 W

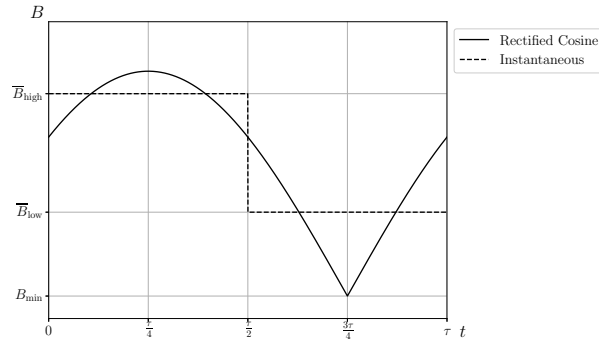
profile was higher ($\bar{B}_{low,RC} > \bar{B}_{low,IT}$). This represents common design scenarios: a constant low-valued plateau for the magnetic field for instantaneous-like magnetic profiles [19,20], or a low peak for the rectified cosine profile [21]. For the other comparison method, the low level of the instantaneous profile was increased ($B_{min,IT} > B_{min,RC}$) in order to keep the same average ($\bar{B}_{low,RC} = \bar{B}_{low,IT}$).

In addition, simulations were carried out for various values of blow fraction; the rectified cosine profile can benefit from a smaller blow fraction because this can concentrate the flow during the periods of very high or low fields. In this section, all results use the critical value of blow fraction that maximized the cooling capacity: fluid flowing during the entire period for the instantaneous profile, and only during 60 % of the period (the smallest blow fraction tested) for the cosine profile; this latter case is shown in Figure 6.

Figure 7 shows the cooling capacity attained by the device at a frequency of 1 Hz and different utilizations, for both comparison methods. The horizontal axis shows the average



(a) Same minimum



(b) Same average

Fig. 5: Comparison methods for the instantaneous and rectified cosine profiles

value during the high field region. For Fig. 7a, the instantaneous profile almost always yields a higher performance, while for Fig. ?? the rectified cosine profile generates higher cooling capacities. Since the average field during the hot cycle (high field stage) is the same, the main difference is due to the low magnetic field levels. For the “same minimum” comparison, the instantaneous profile is capable of keeping the magnetic field at low levels for the whole half-cycle, which is beneficial for performance; for $\Phi = 1.0$ and $\bar{B}_{\text{high}} = 1.40\text{T}$, the cooling capacity for the instantaneous profile is 196.3% higher than for the cosine profile. As demonstrated by [12], a higher average magnetic field during the low-field stage increases

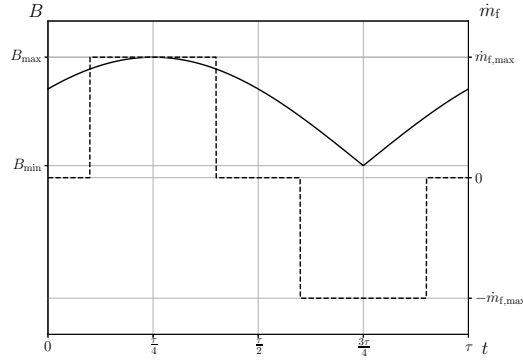
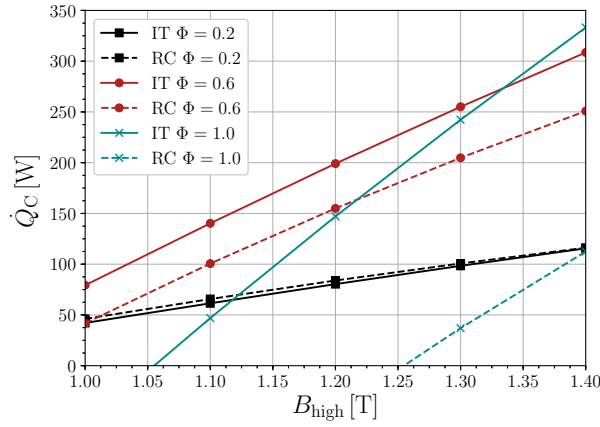


Fig. 6: Rectified cosine magnetic profile and the instantaneous flow profile with blow fraction of 60 %

the solid temperature and consequently results in warmer fluid entering the cold heat exchanger, representing a thermal loss. In the “same-average” comparison, the cosine profile is capable of achieving much lower levels (since its minimum value is fixed), therefore providing more cooling power. However, as explained before, this analysis serves mainly the purpose of illustrating the influence of low magnetic field variation, by looking at two hypothetical scenarios. More complex magnetic circuit geometries are required to generate the instantaneous magnetic profile with a low magnetic field close to 0.

The only exception in the “same minimum” comparison is seen for the lowest utilization of $\Phi = 0.2$, where the performance is slightly better for the RC profile. Since the blow fraction for the cosine is lower, the mass flow rate is higher in the latter for the same utilization (cf. Eq. (12)). This increases the heat transfer rate, as previously explained — outweighing the effects of the magnetic field.

The same analysis, but in terms of the coefficient of performance, is shown in Figure 8. For the “same average” analysis, the COP results show the same trends as the cooling capacity. However, for the somewhat more realistic analysis where the minimum of both profiles

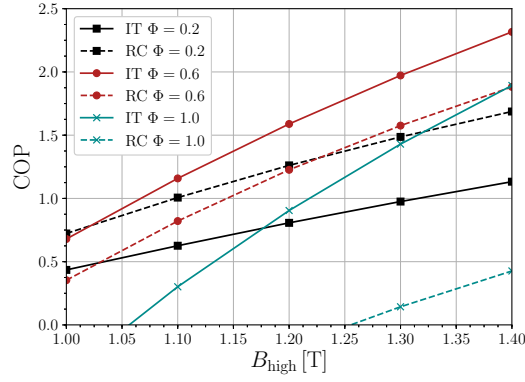


(a) Same minimum

Fig. 7: Cooling capacity as a function of the average high magnetic field, for different utilizations. “IT”: instantaneous (blow fraction of 100 %); “RC”: rectified cosine (blow fraction of 60 %), for both comparison methods.

are the same, the rectified cosine profile yields better results for small values of utilization. This is due to a lower pumping power, as the mass flow rate for the cosine profile is slightly higher, but also flows for a shorter period of time. Since in this region the cooling capacity for the RC profile can be close to or higher than the IT profile (cf. Fig. 7a), the coefficient of performance becomes higher for the rectified cosine profile.

In general, considering the goal of achieving target requirements for the cooling capacity, AMRs operating with the instantaneous magnetic profile generate better performance results. As can be seen in Fig. 7, an instantaneous profile with the lowest possible value of B_{min} and the highest possible value of B_{max} , with a flow profile occupying the whole cycle with average values of utilization, results in the highest values of cooling capacity among all simulations.



(a) Same minimum

Fig. 8: Coefficient of performance as a function of the average high magnetic field, for different utilizations. “IT”: instantaneous (blow fraction of 100 %); “RC”: rectified cosine (blow fraction of 60 %), for both comparison methods.

The rectified cosine profile, found in compact systems using Halbach arrays, can surely benefit from reducing the blow fraction, both in terms of cooling capacity and temperature span. However, for the typical parameters evaluated in this Thesis, even if the blow fraction is optimized for the “RC” profile, the “IT” profile still yields better results.

3.1.1 Analysis of the instantaneous profile

As shown in the previous section, the instantaneous profile generally yields the highest values of cooling capacity. Therefore, in this section, a more detailed analysis of this profile has been carried out, where the maximum field in ?? is varied, while the minimum value is kept at 0.05 T. Figure 9 shows the cooling capacity as a function of the utilization, for several levels of the maximum magnetic field and two different operating frequencies. Because of the conflict between a low heat transfer rate for flow rates that are too low and losses in regenerator effectiveness in flow rates that are too high, there are critical values of utilization

that maximize the cooling capacity, and this critical values increases with the magnetic field. For higher magnetic fields, the increase in the MCE surpasses the loss of effectiveness, and one can go to higher flow rates without losing performance. It can also be seen in Fig. 9 that at higher frequencies the values of cooling power are higher, and also the critical values of utilization are lower; however, this is usually achieved at the expense of a higher power consumption in AMR devices at higher frequencies [22,23].

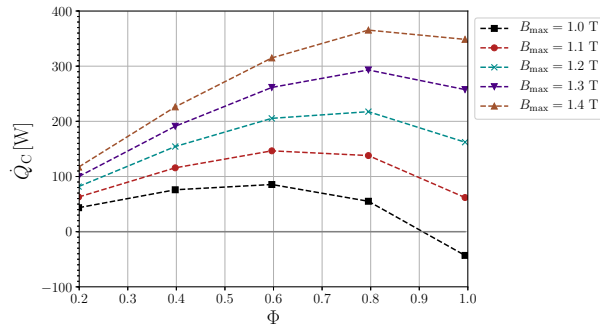
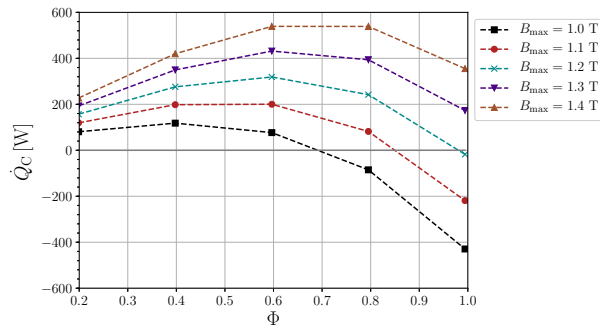
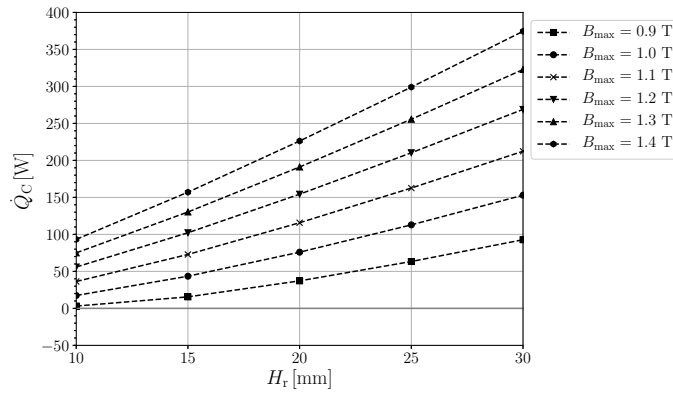
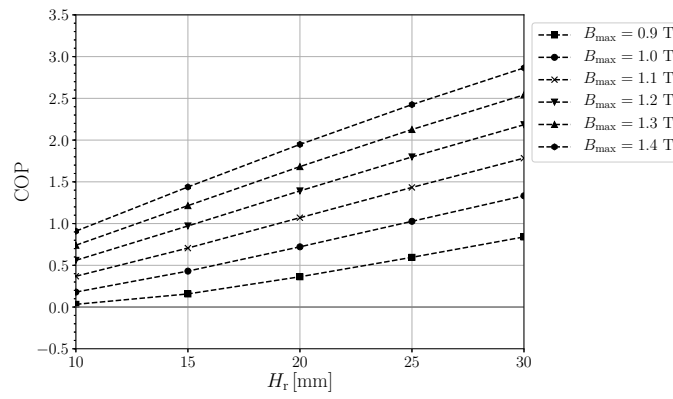
(a) $f = 1 \text{ Hz}$ (b) $f = 2 \text{ Hz}$

Fig. 9: Cooling capacity as a function of utilization, for various values of the high magnetic field for the instantaneous profile



(a) Cooling capacity



(b) Coefficient of performance

Fig. 10: Performance metrics as a function of the regenerator height (all other parameters were set as in Table 1, for utilization factor of 0.4) for various values of the high magnetic field of the instantaneous profile

The parameters in Table 1 were chosen from preliminary simulations, so they are not optimal. To understand the impact of the regenerator geometry on the performance with the instantaneous profile, the regenerator height was varied in Fig. 10, and all other parameters from Table 1 were kept fixed and with $\phi = 0.4$. As expected, higher magnetic fields allow for smaller regenerators (hence more compact systems) to achieve a desired cooling capacity.

For instance, to achieve a capacity of 100 W, increasing the field from 1.0 to 1.2 T results in regenerators that are 36 % smaller. Comparing results for cooling capacity and coefficient of performance, the trends are largely the same, as the former is more sensitive to variations in the magnetic field and regenerator height than the components of power.

3.2 In-depth analysis of the magnetic ramp profile

Based on the better performance of the instantaneous profile, the ramp profile is assumed as a suitable target profile for the design of magnetic refrigerators, and will be analyzed in this section.

Moving towards a more realistic model, casing losses are included, using the model from [11]. The bed is enclosed in a solid casing of thickness h_{csg} , and two air layers of thickness h_{air} separate the AMR and its casing from the inner and outer magnet cylinders.

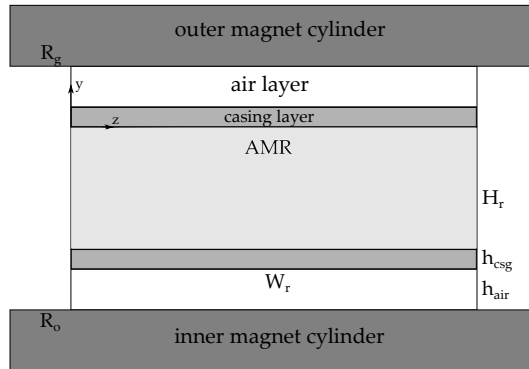


Fig. 11: Model for the casing losses in regenerators

Preliminary analyses carried out by [24] using the losses model described in ?? showed that a stainless steel casing with a thickness of $h_{\text{csg}} = 0.5 \text{ mm}$ is thick enough to ensure

mechanical integrity and easy manufacturing, while being thin enough to accommodate the material with a low thermal conductivity.

In addition, in the present study, an air gap clearance thickness was set at $h_{\text{air}} = 1$ mm. This value gave rise to a peak in cooling capacity due to the compromise between minimizing losses and maximizing the magnetocaloric mass.

The simulations in this section also use multilayer regenerators. A summary of all parameters adopted in this section, including the Curie temperatures and volumetric fractions (relative to the length of the bed) of each layer is presented in Table 2.

Parameter	Value
R_o	40 mm
W_r	30 mm
L_r	85 mm
N_r	8
N_v	16
f	1 Hz
	305.5 K = 32.5 °C
T_C	270.5 K = -2.5 °C
D_p	350 μm
h_{csg}	0.5 mm
h_{air}	1 mm
Casing material	Stainless steel
Number of layers	3
Curie temperatures of each layer	273, 283, 290 K
Length fractions of each layer	20, 20, 60 %

Table 2: Fixed parameters for the AMR simulations used in this chapter

3.2.1 Synchronization between the fluid flow and magnetic profiles

A central point of this Thesis is related to the importance of two characteristic waveforms, the fluid flow and magnetic profiles, and how they affect the performance of a magnetic refrigerator. Several works have independently investigated the synchronization between these profiles [10,25]. Here, the focus is on the parameterization of these waveforms and the characterization of an AMR system with these parameters, in particular the blow fraction (cf. ??) and the magnetization fraction (cf. ??). Figure 12 shows the two profiles that will be used in this section.

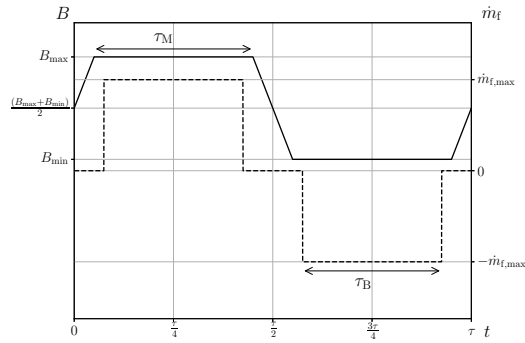


Fig. 12: Comparison between the magnetic ramp profile (solid line) and the instantaneous fluid flow profile (dashed line)

Regarding the magnetic profile, the magnitude of the high value will be varied to investigate the performance of the AMR system, while the minimum will be kept at $B_{\min} = 0.05 \text{ T}$. Ideally, this value should be nil, but it is difficult to achieve complete flux insulation in the low field region, so a finite value of the minimum field is adopted.

3.2.2 Performance curves for varying blow and magnetization fractions

Figure 13 shows the cooling capacity and coefficient of performance of the AMR system for a fixed utilization factor of 0.4 and for a magnetic profile with a maximum at 1.3 T, for variable blow and magnetization fractions. To facilitate the analysis, the results are plotted in terms of the ratio F_M/F_B , with curves for different values of F_B . It is clear that both the cooling capacity and the coefficient of performance exhibit a peak at $F_M = F_B$. Moreover, to the right of the peak, i.e., for higher values of F_M , the reduction of both performance metrics is slower, meaning it is better to have a magnetization plateau wider than the fluid flow plateau, thus confirming the conclusions of ??.

The reduction in performance for $F_M > F_B$ can be explained by an increase in heat leakage through the casing, as the solid begins to lose energy to the environment when the fluid is not flowing. For $F_M < F_B$, the effect discussed in section 3 is present: the fluid begins to flow when the solid is not totally warmed up, losing effectiveness.

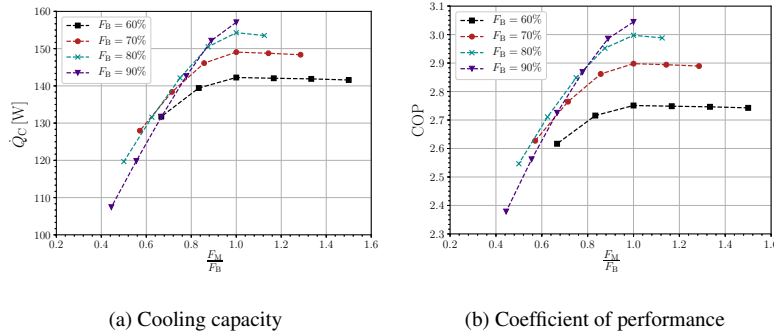


Fig. 13: Performance of the AMR system for various blow and magnetization fractions, utilization of 0.4 and and high magnetic field of 1.3 T

The influence of the utilization is demonstrated in Figure 14, where the cooling capacity is plotted for different utilization factors. For increasing Φ in this range, not only do the overall values of cooling capacity increase, but also the importance of choosing the blow fraction becomes clearer. In these ranges of utilization and blow fraction, the cooling capacity increases because the higher transfer rate associated with higher flow rates dominates over the loss of regenerator effectiveness.

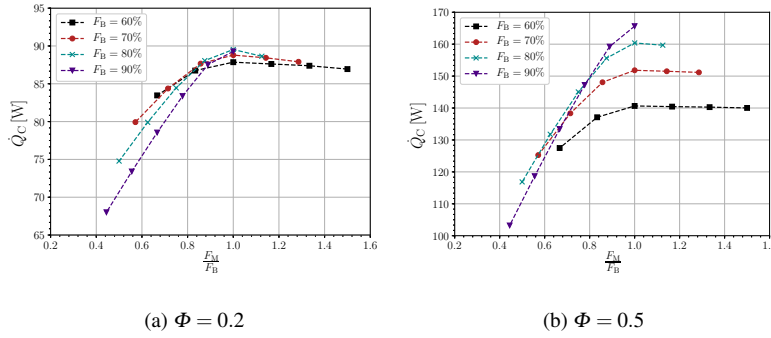


Fig. 14: Influence of utilization on the cooling capacity of the AMR system for various blow and magnetization fractions, with high magnetic field of 1.3 T

The above results can be evaluated from another point of view with Figure 15, where the coefficient of performance is plotted as contour levels. This type of map is useful because, since B_{\min} and τ are fixed, each point in this graph completely characterizes a magnetic ramp profile, and each subplot with fixed Φ and F_B characterizes the fluid flow profile. As expected, the performance increases for the higher values both B_{\max} and F_M , where the magnetic ramp profile tends to the instantaneous magnetic profile with a large amplitude. Confirming the previous trends, the results are less sensitive to the magnetization fraction when $F_M \geq F_B$.

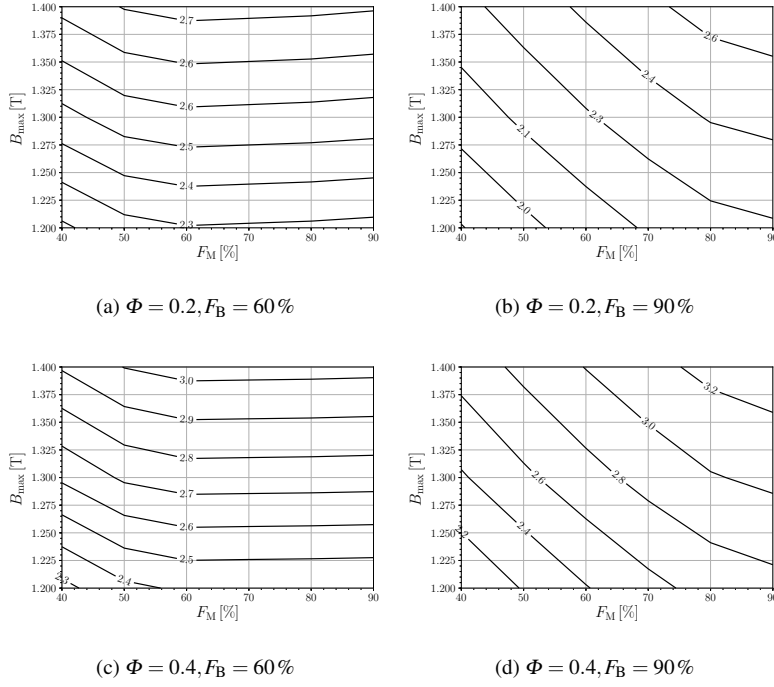


Fig. 15: Influence of utilization and blow fraction on the coefficient of performance of the AMR system for varying high magnetic field and magnetization fraction

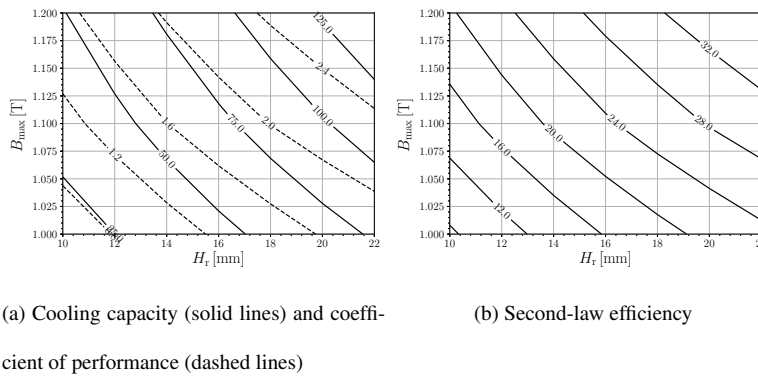
3.2.3 Geometric analysis of the regenerators using the ramp magnetic profile

All previous results assumed a fixed regenerator geometry, with the goal of identifying the optimal fluid and magnetic profile parameters. It became clear that the magnetization fraction should be as large as possible, but that makes it more difficult to design a magnetic circuit based on permanent magnets. The value of $F_M = 70\%$ is then chosen as a compromise, with a corresponding $F_B = F_M$. The mean value of the utilization factor of $\Phi = 0.4$ is also chosen as reference in the next results.

In this section, the effect of the regenerator height is evaluated. The results will complement those for the air gap height that will be shown in ?? concerning the design of the

magnetic circuit. The importance of the air gap height as a coupling parameter between the geometric design of the regenerators and the magnetic circuit was explored using a simplified model in ?? and using the instantaneous magnetic profile in subsection 3.1.1. The results to be shown here use the magnetic ramp profile studied in depth in this present chapter.

Figure 16 shows the cooling capacity, coefficient of performance and second-law efficiency for varying magnetic field and regenerator height. As expected, larger regenerators can produce the desired performance with lower magnetic fields. It can also be seen that this configuration for an AMR system can achieve values of η_{2nd} compatible with conventional vapor compression systems [26,27], although these numerical results do not include mechanical losses.



4 Final considerations

To the authors' knowledge, this is the first study where magnetic profiles for AMR model are mathematically modeled and the model parameters are changed in a systematic way.

The instantaneous profile yields higher cooling capacity, even by reducing the blow fraction on rectified cosine, up to levels achieved by pumping and valving systems, mainly restricted by valve opening times

The ramp profile is a feasible approximation for the instantaneous profile, and can be optimized for increasing cooling capacity. In particular, by synchronizing the plateau durations between fluid and magnetic profiles.

Acknowledgements The authors duly acknowledge the financial support from CNPq (Grant no. 443696/2014-4), Capes (PTI program, Process no. 88887.194773/2018-00), Embraco and the EMBRAPA Unit Polo/UFSC.

References

1. P. Bansal, E. Vineyard, O. Abdelaziz, *International Journal of Sustainable Built Environment* **1**, 85 (2012)
2. IIR. 36th informatory note on refrigeration technologies: Flammable refrigerants. Available at http://www.iifir.org/userfiles/file/publications/notes/NoteTech_36_EN_nkyix2fcj7.pdf (2017). Accessed on October 30th, 2018
3. S. Lionte, M. Risser, C. Vasile, L. Elouad, C. Muller, *International Journal of Refrigeration* **85**, 303 (2018). DOI 10.1016/j.ijrefrig.2017.10.009
4. A. Smith, C.R.H. Bahl, R. Bjørk, K. Engelbrecht, K.K. Nielsen, N. Pryds, *Advanced Energy Materials* **2**, 1288 (2012)
5. A. Kitanovski, U. Plaznik, J. Tušek, A. Poredoš, *International Journal of Refrigeration* **37**, 28 (2014)
6. R. Teyber, P.V. Trevizoli, I. Niknia, T.V. Christiaanse, P. Govindappa, A. Rowe, *International Journal of Refrigeration* **74**, 38 (2017)
7. A.T.D. Nakashima, S.L. Dutra, P.V. Trevizoli, J.R. Barbosa, Jr., *International Journal of Refrigeration* **93**, 236 (2018)

8. F.P. Fortkamp, D. Eriksen, K. Engelbrecht, C.R.H. Bahl, J.A. Lozano, J.R. Barbosa, Jr., *International Journal of Refrigeration* **91**, 46 (2018). DOI 10.1016/j.ijrefrig.2018.04.019
9. J. Tušek, A. Kitanovski, I. Prebil, A. Poredoš, *International Journal of Refrigeration* **34**(6), 1507 (2011). DOI 10.1016/j.ijrefrig.2011.04.007
10. R. Bjørk, K. Engelbrecht, *International Journal of Refrigeration* **34**, 192 (2011). DOI 10.1016/j.ijrefrig.2010.07.004
11. P.V. Trevizoli, A.T. Nakashima, J.R. Barbosa, Jr., *International Journal of Refrigeration* **72**(206-217) (2016)
12. P.V. Trevizoli, J.R. Barbosa, Jr., A. Tura, D. Arnold, A. Rowe, *Journal of Thermal Science and Engineering Applications* **6** (2014)
13. D. Eriksen, K. Engelbrecht, C.R.H. Bahl, R. Bjørk, K.K. Nielsen, *Applied Thermal Engineering* **103**, 1 (2016)
14. K.K. Nielsen, J. Tusek, K. Engelbrecht, S. Schopfer, A. Kitanovski, C.R.H. Bahl, A. Smith, N. Pryds, A. Poredos, *International Journal of Refrigeration* **34**, 603 (2011)
15. S.A. Klein. EES — Engineering Equation Solver, Professional Version v9.339. F-Chart Software (2013). Available at <http://fchart.com>.
16. A.T.D. Nakashima, S.L. Dutra, G. Hoffmann, J.A. Lozano, J.R. Barbosa, Jr., in *Proceedings of the 8th International Conference on Caloric Cooling (Thermag VIII)* (Darmstadt, Germany, 2018)
17. P.O. Cardoso, M.C. Destro, M.G. Alvarez, J.A. Lozano, J.R. Barbosa, Jr., V.J. de Negri, in *Proceedings of the 16th Brazilian Congress of Thermal Sciences and Engineering* (Vitória, 2016)
18. D. Eriksen, K. Engelbrecht, C.R.H. Bahl, R. Bjørk, K.K. Nielsen, A.R. Insinga, N. Pryds, *International Journal of Refrigeration* **58**, 14 (2015)
19. A.R. Insinga, Optimising magnetostatic assemblies. Department of Energy Conversion and Storage, Technical University of Denmark (2016)
20. M.A. Benedict, S.A. Sherif, D.G. Beers, M.G. Schroeder, *Science and Technology for the Built Environment* **22**(5), 520 (2016). DOI 10.1080/23744731.2016.1185889
21. P.V. Trevizoli, J.A. Lozano, G.F. Peixer, J.R. Barbosa, Jr., *Journal of Magnetism and Magnetic Materials* **395**, 109 (2015)
22. T. Lei, K. Engelbrecht, K.K. Nielsen, C.T. Veje, *Applied Thermal Engineering* **111**, 1232 (2017)
23. I. Niknia, O. Campbell, T.V. Christiaanse, P. Govindappa, R. Teyber, P.V. Trevizoli, A. Rowe, *Applied Thermal Engineering* **106**, 601 (2016). DOI 10.1016/j.applthermaleng.2016.06.039

-
24. G.F. Peixer, J.A. Lozano, J.R. Barbosa, Jr. Performance evaluation of AMRs using different casings. Book of Abstracts for the Danish Days on Caloric Materials and Devices (2017)
 25. A.T. Nakashima, S.L. Dutra, J.R. Barbosa, Jr., P.V. Trevizoli, in *Proceedings of the 9th World Conference on Experimental Heat Transfer, Fluid Mechanics and Thermodynamics* (Iguazu Falls (Brazil), 2017)
 26. C.J.L. Hermes, C. Melo, International Journal of Refrigeration **31**(8), 1341 (2008). DOI 10.1016/j.ijrefrig.2008.04.003,
 27. C.O.R. Negrão, C.J.L. Hermes, Applied Energy **88**(9), 3051 (2011). DOI 10.1016/j.apenergy.2011.03.013